Image Dehazing by Artificial Multiple-Exposure Image Fusion

A. Galdran[a,*]

[a]*INESC TEC Porto, R. Dr. Roberto Frias, 4200 Porto, Portugal*

Abstract

Bad weather conditions can reduce visibility on images acquired outdoors, decreasing their visual quality. The image processing task concerned with the mitigation of this effect is known as image dehazing. In this paper we present a new image dehazing technique that can remove the visual degradation due to haze without relying on the inversion of a physical model of haze formation, but respecting its main underlying assumptions. Hence, the proposed technique avoids the need of estimating depth in the scene, as well as costly depth map refinement processes. To achieve this goal, the original hazy image is first artificially under-exposed by means of a sequence of gamma-correction operations. The resulting set of multiply-exposed images is merged into a haze-free result through a multi-scale Laplacian blending scheme. A detailed experimental evaluation is presented in terms of both qualitative and quantitative analysis. The obtained results indicate that the fusion of artificially under-exposed images can effectively remove the effect of haze, even in challenging situations where other current image dehazing techniques fail to produce good-quality results. An implementation of the technique is open-sourced for reproducibility (`https://github.com/agaldran/amef_dehazing`).

Keywords: Image Dehazing, Fog Removal, Multi-Exposure Image Fusion, Gamma Correction, Image Fusion, Laplacian Pyramid

1. Introduction

Images acquired outdoors are sometimes degraded by a decrease in visibility caused by small particles suspended in the atmosphere. This physical phenomenon is known as haze or fog, and its main effect is the attenuation of the radiance along its path towards the camera. As a result, acquired images and videos suffer from loss of contrast and color quality degradation, limiting visibility on far away areas in the scene. This lack of visibility can hinder the performance of computer vision systems designed to operate on clear conditions and also decreases visual pleasantness of image contents for users of standard consumer cameras.

The task of restoring the visual quality of weather-degraded images has been increasingly drawing attention in recent years. In this context, the image processing problem concerned with removing the effect of foggy conditions is known as image dehazing. The availability of effective image dehazing techniques can have a positive impact in computer vision tasks that need to be performed in outdoor scenarios, such as surveillance [1], remote sensing [2, 3], or autonomous driving under bad-weather conditions [4].

Haze degradation is known to increase with respect to depth in the imaged scene. However, due to the ambiguity introduced by the lack of depth information in two-dimensional images, early solutions to remove haze relied on external sources of information [5, 6, 7]. Unfortunately, this external information is not usually available in generic situations, limiting the applicability of this kind of techniques.

Single-image dehazing approaches were introduced to overcome this obstacle. A single-image dehazing technique assumes no external knowledge of the scene an image depicts. However, since haze is a depth-dependent phenomenon, the resulting image degradation is spatially-variant, with different areas of the image being more affected. In this situation, unavailable depth information is typically alleviated by resorting to physical models of haze formation. Unfortunately, even simplified physical models need to hold depth information, either implicitly or explicitly. As a result, most existing single-image dehazing methods impose prior information on the image the user expects to obtain, *e.g.* an increased contrast or less attenuated colors [8, 9].

The main contribution of this paper is an alternative single image dehazing method that employs physical models of haze formation only as an inspiration to understand characteristics of the image we expect to obtain. We consider single-image haze removal as a spatially-varying contrast and saturation enhancement problem on which different areas of the image require distinct levels of processing. Hence, a new image dehazing technique aiming at increasing visual quality only on those areas is built. This is achieved by artificially underexposing the hazy image through a series of gamma-correction operations. The resulting set of progressively underexposed images contains regions with increased contrast and saturation. To further account for the spatially-varying nature of weather degradation, a simple and efficient

*Corresponding author
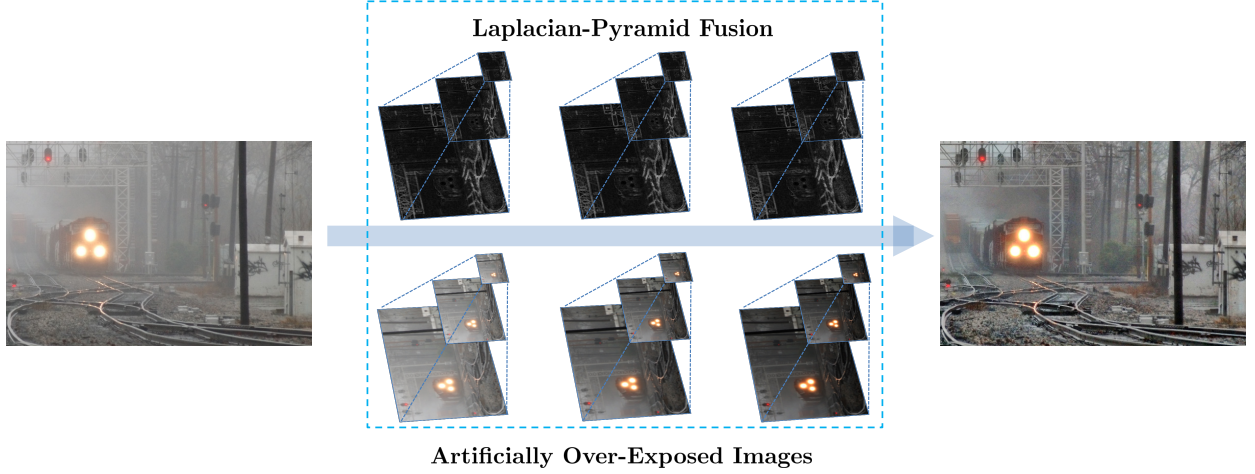Email address: `adrian.galdran@inesctec.pt` (A. Galdran)

Figure 1: A schematic representation of the proposed image dehazing technique.

multi-scale fusion scheme is applied in order to collect from each image the best-quality areas and combine them into a single haze-free output. A visual description of the method developed in this paper is shown in Fig. 1.

2. Related Work

When approaching single-image dehazing as an image restoration problem, most existing methods solve the following physical model of haze degradation, due to H. Koschmieder [10]:

$$\mathbf{I}(x) = t(x) \cdot \mathbf{J}(x) + (1 - t(x)) \cdot \mathbf{A}, \qquad (1)$$

where $\mathbf{I}(x) = (\mathbf{I}^R(x), \mathbf{I}^G(x), \mathbf{I}^B(x))$ is the degraded image, $\mathbf{J}(x)$ is a haze-free image, $t(x)$ is the medium transmission describing the amount of light that reaches the receiver, which is inversely related to depth, and $\mathbf{A}$ is a constant (RGB)-vector known as atmospheric light. The combined degradation of transmission and atmospheric light, *i.e.* the term $\mathbf{A}(1-t(x))$, is usually known as *airlight*, and it accounts for a possible shift in scene colors due to the presence of different sources of illumination other than sunlight.

Given a hazy image $\mathbf{I}(x)$, there are many possible solutions $\mathbf{J}(x)$ verifying Kochsmieder's model, *i.e.* the inversion of eq. (1) is an under-constrained problem. In order to find a meaningful solution, prior information is typically imposed to infer $t(x)$ and $\mathbf{A}$. When these have been estimated, the above equation can be inverted:

$$\mathbf{J}(x) = \frac{\mathbf{I}(x) - \mathbf{A}}{t(x)} + \mathbf{A} \qquad (2)$$

The most popular restriction on $\mathbf{J}(x)$ is the Dark Channel Prior (DCP), introduced in [8], which enforces the presence of at least a low-intensity pixel in some color channel of a local neighborhood around every pixel. The DCP has been extended in many directions [11]. Other alternatives exist, such as imposing maximal local contrast/saturation [12], or a specific distribution of color pixels in the RGB space [13, 14]. A recent review on this topic can be found in [15].

Kochschmieder model is also leveraged in a second family of image dehazing techniques, those based on machine learning techniques. In this case, instead of directly trying to estimate $t(x)$, a mapping between a hazy image and its depth is learned from data. This can be achieved by first creating synthetic depth maps only from hazy images as in [16], or by injecting synthetic fog on a set of haze-free images for which true depth information is known [17]. Once a dataset of hazy images and corresponding ground-truth is built, a mapping linking images to plausible transmission maps can be learned by means of a given machine learning model, from simple linear techniques [9] to Convolutional Neural Networks [18]. The resulting transmission map estimate can be applied afterwards to invert eq. (1).

Yet a third family of image dehazing techniques consists of methods considering dehazing as an image enhancement problem. In this case, it is assumed that the image formation model of eq. (1) is useful to understand the relationship between a hazy image acquired by a camera under bad weather conditions and a corresponding haze-free image. However, the goal is not to estimate $t(x)$ nor A, in order to invert the model, but rather to produce a good-quality dehazed image $\mathbf{J}(x)$. This is accomplished by some kind of spatially-variant contrast enhancement process, being Retinex-based techniques the most popular approach [19, 20]. Fusion-based techniques are an important subset of these methods, closely related to the technique introduced in this paper. Fusion-based methods like [21] or [22] have several advantages over standard image dehazing approaches. Firstly, they typically perform per-pixel, instead of patch-based computations, avoiding costly refinement stages [23]. Secondly, per-pixel computations are usually more efficient and amenable to parallelization.

The image dehazing method proposed in this work is based on fusing the result of a sequence of applications of gamma corrections. Gamma correction has been widely explored in the past for image enhancement tasks. In [24], the authors merged gamma corrections of conventional histogram

equalization in order to achieve more effective contrast improvement. In [25], an iterative method, automatically adapted to the kind of degradation the image suffered, was proposed. Adaptive gamma correction was also adopted in [26], achieving image content-dependence by devising a piece-wise power transform through the incorporation of a cumulative histogram into a weighting distribution. However, even if these methods are adaptive with respect to the image content and intensities, they remain global image transformations.

Other image processing tasks, *e.g.* color registration on image sequences [27], have been approached with extensions of basic gamma correction. However, image dehazing through gamma correction has been hardly explored in the past. In [28], the authors proposed an adaptive gamma correction scheme to refine the transmission map $t(x)$ before inverting model (1). The same idea was further improved in [29] through Laplacian-based techniques. In [30] gamma correction was explored in conjunction with other contrast adjustment techniques in order to rectify the intensities on the negative of a hazy image in an efficient manner.

3. Artificial Multi-Exposure for Image Dehazing

The purpose of this paper is to build a spatially-varying image enhancement technique capable of removing the visual effect of haze, bypassing the need of estimating transmission and airlight in eq. (1). However, there is underlying information in Koschmieder's model that can be useful to understand the kind of solution we should expect to obtain. To see this, let us consider an input hazy image $\mathbf{I}(x)$ with intensity values varying in $[0, 1]$. Then, any solution $\mathbf{J}(x)$ to the image dehazing problem needs to contain intensity values lower than $\mathbf{I}(x)$. This can be shown by simply rearranging eq. (1) as:

$$t(x) = \frac{\mathbf{A} - \mathbf{I}(x)}{\mathbf{A} - \mathbf{J}(x)}. \tag{3}$$

Since $t(x) \in [0, 1]$, it follows from eq. (3) that $\mathbf{A} - \mathbf{I}(x) \leq \mathbf{A} - \mathbf{J}(x)$, and it can be concluded that $\mathbf{J}(x) \leq \mathbf{I}(x) \forall x$.

According to the above observation, the technique introduced in this paper proposes to make use of the information present in a set of over-exposed versions $\mathbf{E} = \{\mathbf{I}^1(x), \mathbf{I}^2(x), ..., \mathbf{I}^n(x)\}$ of the original hazy image $\mathbf{I}(x)$. Underexposing $\mathbf{I}(x)$ will always lead to the presence of decreased intensities. However, when $\mathbf{I}(x)$ is globally underexposed, not every region on it contains useful information, since insufficient exposure will darken $\mathbf{I}(x)$ too much. For this reason, all images in $\mathbf{E}$ are fused by means of a simple and efficient multiple-exposure fusion strategy relying on a Laplacian pyramid decomposition of the set of over-exposed images. The resulting image is a haze-free version of $\mathbf{I}(x)$. In the next sections, the different steps of this procedure are explained in detail.

3.1. *Artificial Exposure Modification via Gamma Correction Transforms*

In photography, exposure is defined as the amount of light that is allowed to enter the camera and reach the sensors while acquiring an image [31]. Exposure can be adjusted during acquisition by varying the shutter speed of the camera or its aperture, but it is typically hard to achieve a generally optimal exposure for any scene. Moreover, different areas of the imaged scene may require completely distinct exposures. The reason for this is the large *dynamic range* of the light reaching the camera.

The difference between the brightest and darkest intensity values that a camera can register is called dynamic range. Most consumer cameras acquire low dynamic range images, covering few orders of magnitude. As a result, when capturing an image of a scene reflecting a high dynamic range of light, a short exposure will allow the camera to correctly capture details in the brightest areas of the image. However, on the same conditions the camera will be unable of properly depicting details in dark regions, and the corresponding image areas will be underexposed. In the same way, if a long exposure is used, dark region details will become apparent, but bright regions will become white, *i.e.* these areas will be overexposed. Typically no single exposure time will be useful for both kind of regions.

In controlled illumination situations, a possible solution is to shed artificial light on dark areas of the scene to reduce its dynamic range. A second approach consists of acquiring several images of the same scene under different exposures and combining the information on all these images into a single one containing sharp details both on bright and dark regions. This image processing problem is known as Multiple Exposure Fusion (MEF). MEF has been widely studied in the past, and will be briefly discussed in section 3.2 below.

Unfortunately, most of the times the user has no control on the illumination of the scene, or the image has already been captured and stored, with no option to acquire extra differently exposed images on the same scene. In this case, an alternative solution consists of digitally adjusting the exposure of the image. One of the simplest algorithms to manipulate exposure is gamma correction. This consists of globally modifying the intensities on an image following a power-function transform:

$$\mathbf{I}(x) \mapsto \alpha \cdot \mathbf{I}(x)^\gamma, \tag{4}$$

where α, γ are real positive numbers. Power transform operations were initially applied to correctly reproduce luminance on CRT televisions [31]. However, gamma correction is still used nowadays for optimized image storage. It is well-known that differences in dark areas of an image are perceptually more noticeable than the same differences in bright areas. Hence, gamma-corrected digital signals are quantized in such a way that wider quantization intervals are employed at higher luminance ranges, where changes are less noticeable. Conversely, narrower intervals are applied for darker regions, where details can be more perceptible, as illustrated in Fig. 2. Note that, if we adopt as simple definition of image contrast for a given region Ω inside the image domain:

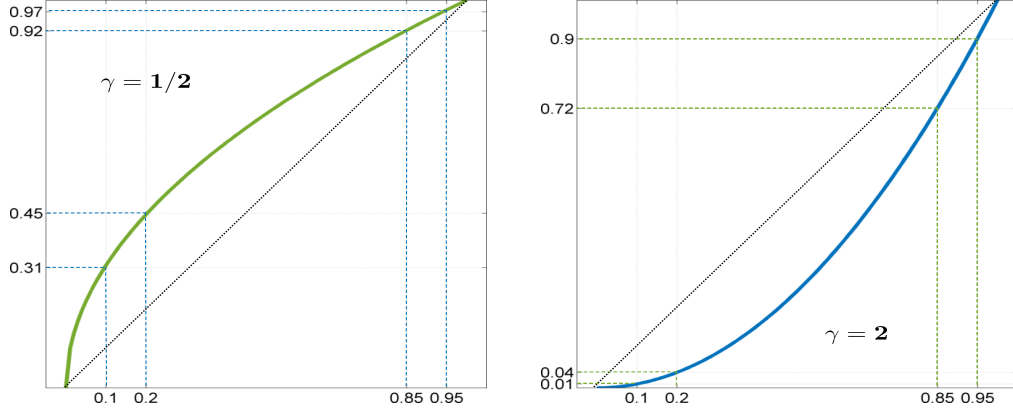$$\mathscr{C}(\Omega) = I_{\max}^\Omega - I_{min}^\Omega, \tag{5}$$

3

Figure 2: Dynamic range expansion/compression due to power transforms. Left: For $\gamma < 1$, brighter intensities are compressed while darker intensities are expanded. Right: conversely, for $\gamma > 1$, brighter intensities are allocated in a wider range after transformation, while darker intensities are mapped to a compressed interval.

where $I_{\max}^{\Omega} = \max\{I(x) \mid x \in \Omega\}$ and $I_{\min}^{\Omega} = \min\{I(x) \mid x \in \Omega\}$, then it can be easily shown that, *e.g.* for $\gamma > 1$, given a region containing bright values like in the right side of Fig. **??**, its contrast as measured by eq. (5), will be increased after gamma correction, as shown in the right side of Fig. **??**.

Optimal gamma-transformations and methods for estimating the γ-coefficient applied by a camera while storing an image have been explored in the past [32, 33]. However, in this paper we are interested in the visual effect that this transformation can achieve on a digital image. In this sense, it is worth noting that gamma correction allows to globally increase or reduce exposure on a given image. Unfortunately, the application of eq. (4) leads to a global effect by which properly-exposed areas of the image become deteriorated, as shown in Fig. **??**. However, as discussed in the next section, it is still possible to identify and fuse each of the image areas in order to obtain a fused image containing well-exposed areas across its entire domain.

3.2. Multi-Exposure Image Fusion

Since its introduction in [34], Multiple Exposure Fusion (MEF) has been largely investigated. However, the large majority of MEF algorithms can be grouped into a single framework, that aims at finding the optimal weights $\mathbf{W}_k$ in the following formula:

$$\mathbf{J}(x) = \sum_{k=1}^{K} \mathbf{W}_k(x)\mathbf{E}_k(x), \qquad (6)$$

where K is the number of differently exposed available images $\mathbf{E}_k(x)$, and $\mathbf{J}(x)$ is a globally well-exposed image, resulting from the combination of the different correctly-exposed areas in $\mathbf{E}_k$. Weights $\mathbf{W}_k$ are normalized so that $\sum_k \mathbf{W}_k(x) = 1 \; \forall x$, in order to keep the intensities of $\mathbf{J}(x)$ in range. Some variants of this approach avoid pixel-wise weighting by computing block-wise weights $\mathbf{W}_k$, or solve eq. (6) in a transformed domain [35, 36].

Many techniques have been proposed to compute optimal $\mathbf{W}_k(x)$ in eq. (6). Typically a multi-resolution strategy is

applied to avoid blending artifacts. This idea was introduced in [37] by means of a Laplacian Pyramid decomposition, and is recurrent in the literature. In [38], contrast, saturation, and well-exposedness were employed as cues to detect correctly exposed regions before performing a Laplacian multi-scale fusion. Also, in [39] gradient information and the structure tensor were used for the same purposes, and in [40, 41] edge relevance was taken into consideration for either weighting image areas or refining initial weight estimates. This can be achieved by means of different edge-preserving filters, *e.g.* bilateral or guided filters.

To avoid the appearance of visual artifacts, the multi-scale approach for image fusion based on the classical Laplacian pyramid [42] is also followed in this work. Let us assume that a set of maps $\mathbf{W}_k$ indicating the haze-free areas in each image is already available. Directly combining the input multi-exposed images into $\mathbf{J}(x)$ following eq. (6) would result in hard transitions associated to weight maps' borders. In order to combine different scales together, first a Gaussian pyramid is built for each weight map as:

$$\mathbf{W}_k^i = \mathrm{ds}_2\left[\mathbf{W}_k^{i-1}\right], \qquad (7)$$

where $\mathrm{ds}_2[\,\cdot\,]$ corresponds to an operator that convolves an image with a Gaussian kernel, and then downsamples it to half of its original dimensions. Iterating this process N times produces a set of progressively smaller and smoother weight maps $\{\mathbf{W}_k^1, \mathbf{W}_k^2, \dots, \mathbf{W}_k^N\}$.

In a similar way, a Gaussian pyramid $\{\mathbf{E}_k^1, \mathbf{E}_k^2, \dots, \mathbf{E}_k^N\}$ is built for each of the multi-exposed images $\mathbf{E}_k$. Then, a Laplacian pyramid is constructed for each $\mathbf{E}_k$ through the following recursive formula:

$$\mathbf{L}_k^i = \mathbf{E}_k^i - \mathrm{us}_2\left[\mathbf{E}_k^{i+1}\right], \qquad (8)$$

where $\mathrm{us}_2[\,\cdot\,]$ is an operator upsampling an image to twice its size. In the above recursion, we define $\mathbf{L}_k^N = \mathbf{E}_k^N$.

Since $\mathbf{L}_k^i(x)$ captures the frequency content of the original image at scale i, a multi-scale combination of all $\mathbf{E}_k(x)$

can be achieved by combining every image in the K pyramids across-levels and summing-up together the upsampled results. If the source images $\mathbf{E}_k(x)$ are of dimensions $m \times n$, the Laplacian pyramid blending gives:

$$\mathbf{J}(x) = \mathrm{us}_{(m,n)}\big[\mathbf{L}_1^1(x) \cdot \mathbf{W}_1^1(x) + \ldots + \mathbf{L}_K^1(x)\mathbf{W}_K^1(x)\big] + \mathrm{us}_{(m,n)}\big[\mathbf{L}_1^2(x) \cdot \mathbf{W}_1^2(x) + \ldots + \mathbf{L}_K^2(x)\mathbf{W}_K^2(x)\big]$$

(9)

$$+ \ldots + \mathrm{us}_{(m,n)}\big[\mathbf{L}_1^N(x) \cdot \mathbf{W}_1^N(x) + \ldots + \mathbf{L}_K^N(x)\mathbf{W}_K^N(x)\big] = \sum_{i=1}^{N} \mathrm{us}_{(m,n)}\left[\sum_{k=1}^{K} \mathbf{L}_k^i(x) \cdot \mathbf{W}_k^i(x)\right]$$

where $\mathrm{us}_{(m,n)}$ is the operator upsampling any given image to the dimension of $\mathbf{E}_k$. A schematic representation of the Laplacian decomposition scheme is given in Fig. (3).

It is worth noting that different weight selections $\mathbf{W}^k$ in eq. (6) will lead to distinct multi-scale blending results. However, even simple choices can produce visually satisfactory results, as illustrated in Fig. 4. In the next section, a weight selection suitable for the task of image dehazing will be described.

3.3. Image Dehazing by Artificial Multiple Under-Exposed Image Fusion

As illustrated in Fig. (4a), artificially under/overexposing an image and fusing the results in a multi-scale fashion can integrate well-exposed areas from each of the source images. However, for the purposes of this paper, it is of interest to model the fact that a solution to the haze formation in eq. (1) must always decrease intensities. For this reason, we propose to compute only artificially under-exposed images, *i.e.* apply only $\gamma > 1$ in eq. (4). The global effect of this operation is a reduction in brightness. Moreover, subsequent applications of gamma-correction with increasing values of γ can reveal useful visual information on a hazy image.

With the choice of $\gamma > 1$, it can be easily verified that the dehazed image computed by eq. (6) always fulfills the intensity decrease requirement. Consider a set of under-exposure factors $\Gamma = \{\gamma^1, \gamma^2, \ldots \gamma^K \mid \gamma^k > 1\}$. Since $\mathbf{I}(x) \in [0, 1]$, then $\mathbf{I}(x)^{\gamma^k} < \mathbf{I}(x)$ for every pixel x. Due to the weights in eq. (6) being normalized to sum up to 1, we have that:

$$\mathbf{J}(x) = \sum_{k=1}^{K} \mathbf{W}^k(x)\mathbf{I}^k(x) \leq \sum_{k=1}^{K} \mathbf{W}^k(x)\mathbf{I}(x) = \mathbf{I}(x) \qquad (10)$$

The effect of artificially under-exposing a hazy image is illustrated in Fig. (5a) and Figs. (5c) to (5l). It can be appreciated that, in a foggy image, well-exposed regions corresponding to areas closer to the camera can be found. Moreover, by artificially under-exposing the initial image, hazy regions lying further away from the observer can be transformed into well-saturated areas. The main drawback with globally under-exposing a hazy image is that areas that were initially of high visual quality in the first place are completely darkened. The goal thus becomes to build a suitable set of weight

maps modeling the presence of fog on each artificially under-exposed image in order to select from each of them regions with the minimum haze density. Note that, by considering the original image also as an input for the fusion stage, the result of the merging procedure explained below will retain the ability of keeping regions of the image that were naturally dark in the initial scene. In this way, those regions will not be discarded and will end up belonging to both the input image and the dehazed result.

It is well-known that one of the main visual effects of fog is the loss of contrast and saturation, and this has been widely exploited in the literature. For instance, the popular Dark Channel Prior (DCP) imposes that, on a haze-free image, there must always be a dark pixel in a neighborhood around each pixel. Thus, the DCP proceeds by computing local minima both in space and RGB coordinates, building the Dark Channel image as:

$$\mathbf{J}^{\mathrm{dark}}(x) = \min_{c \in \{R,G,B\}} \left(\min_{y \in \Omega(x)} \mathbf{J}^c(y) \right), \qquad (11)$$

where $\Omega(x)$ is a patch centered at pixel x. By imposing that the Dark Channel image contains only low intensities, it is possible to maximize both contrast and saturation on hazy regions. The reason for this is that verifying the DCP on hazy areas requires a local stretching of values in spatial neighborhoods (thereby expanding local contrast) combined with a local stretching of values in the RGB space (resulting in a saturation increase).

However, one of the main disadvantages of the DCP and its variants is that patch-wise computations are necessary in order to robustly estimate contrast and saturation. This creates the need of a costly post-processing of the haze map, typically achieved by the guided filter or similar techniques. To overcome these drawbacks, in this paper we simplify the approach proposed in [38]. In this case, given a source image $\mathbf{E}^k(x) = (\mathbf{E}_k^R(x), \mathbf{E}_k^G(x), \mathbf{E}_k^B(x))$, the contrast $\mathbf{C}_k(x)$ at each pixel x is measured as the absolute value of the response to a simple Laplacian filter, while saturation $\mathbf{S}_k(x)$ on each pixel is estimated by the standard deviation across color channels:

$$\mathbf{C}_k(x) = \frac{\partial^2 \mathbf{E}_k}{\partial x^2}(x) + \frac{\partial^2 \mathbf{E}_k}{\partial y^2}(x), \qquad (12)$$

$$\mathbf{S}_k(x) = \sum_{c \in \{R,G,B\}} \left(\mathbf{E}_k^c(x) - \frac{\mathbf{E}_k^R(x) + \mathbf{E}_k^G(x) + \mathbf{E}_k^B(x)}{3} \right)^2. \qquad (13)$$

Finally, a haze map for each under-exposed image is obtained by simply combining multiplicatively the contrast and saturation maps:

$$\mathbf{W}^k(x) = \mathbf{C}^k(x) \cdot \mathbf{S}^k(x) \qquad (14)$$

The resulting weights are inserted in eq. (6) and the Laplacian multi-scale fusion described in the previous section is performed. This results in a haze-free image integrating well-contrasted regions with rich colors from each source image, as illustrated in Fig. 5b.

It can be experimentally verified that when the input hazy image contains few well-contrasted regions, over-exposed
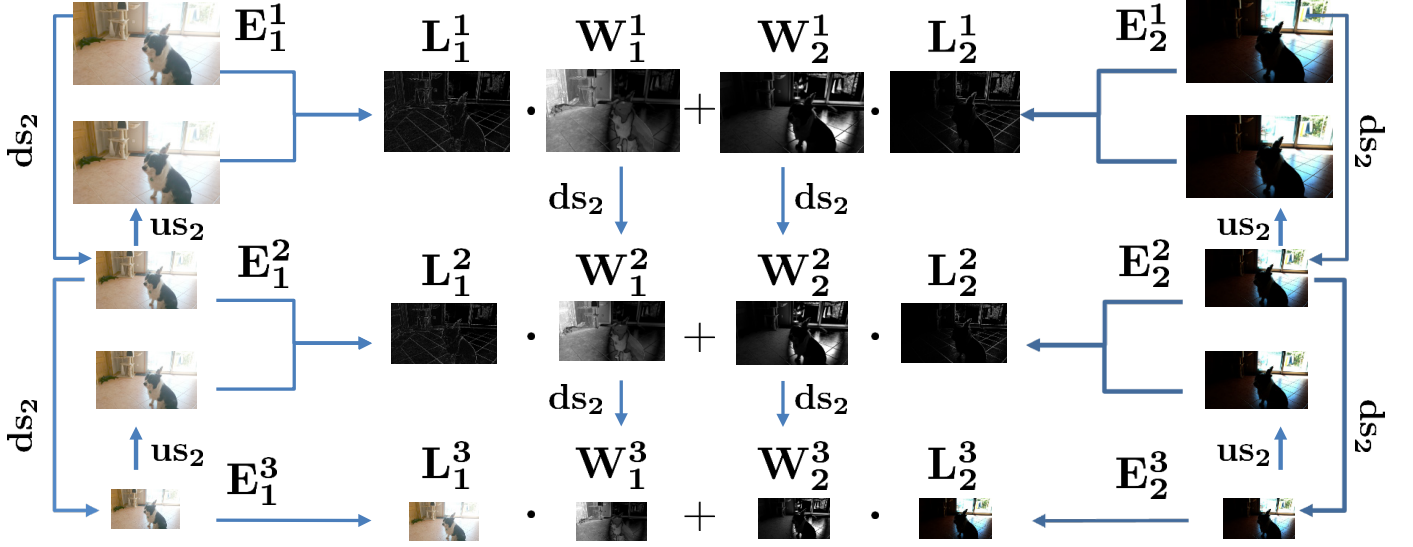
Figure 3: Laplacian pyramid decomposition scheme for the fusion of the multiply-exposed images in Figs. (??) and (??).

images can sometimes produce too dark results. In order to incorporate further contrast in the dehazed result without introducing many extra parameters in the proposed method, a simple contrast-enhanced version of the input image can be added to the original set of artificially under-exposed images. In this case, the popular Contrast-Limited Adaptive Histogram Equalization (CLAHE, [43]) was selected. This algorithm depends on a ßingle relevant parameter, the *clip-range* (amount of local contrast increase that the user decides to allow), and can typically produce over-enhanced results. An example of the application of this extended scheme is presented in Fig. (6). It can be appreciated how the local histogram equalization alters the appearance of regions in the image that were not suffering from contrast or saturation loss, mainly the areas closer to the camera. On the other hand, the contrast provided by CLAHE in far away areas of the scene is effectively incorporated in the final result

on Fig. (6b). Also, the under-exposed images in Figs. (6d), (6e), and (6f) contribute to add properly saturated regions coming from the mid-range depth of the scene into the final result.

4. Experimental Results

In this section we provide extensive evaluation of the performance of the proposed Artificial Multiple Exposure Fusion technique (referred to as **AMEF** from here on) for the task of image dehazing, both in terms of subjective and quantitative evaluation.

4.1. Parameters Setting

The proposed **AMEF** technique for image dehazing has few parameters that need to be adjusted. One of these is
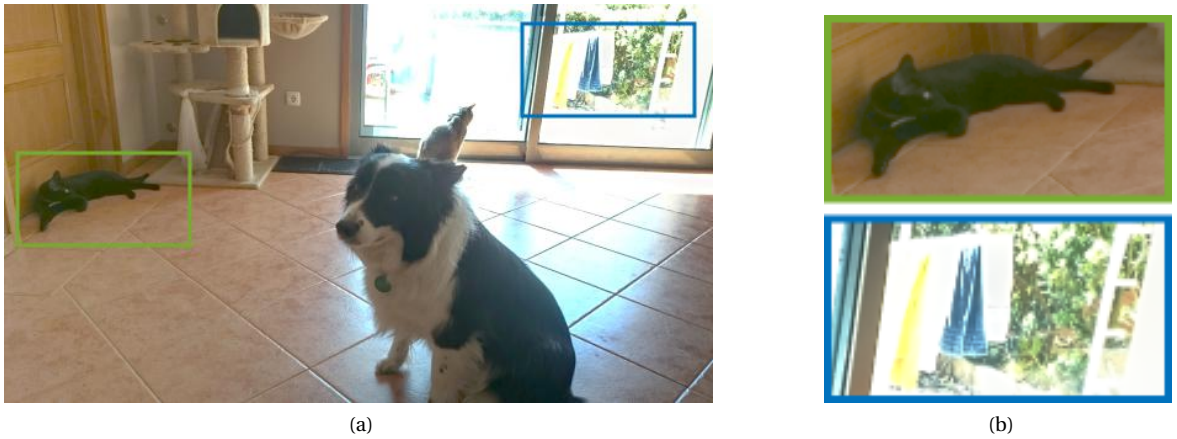

Figure 4: (a) Result of fusing the image in Fig. (??) and the artificially exposed images in Figs. (??) and (??) with weights $\mathbf{W}^k$ consisting of measuring at each pixel contrast as the absolute value of each image's Laplacian. (b) Zoomed-up detail, both regions are correctly exposed.
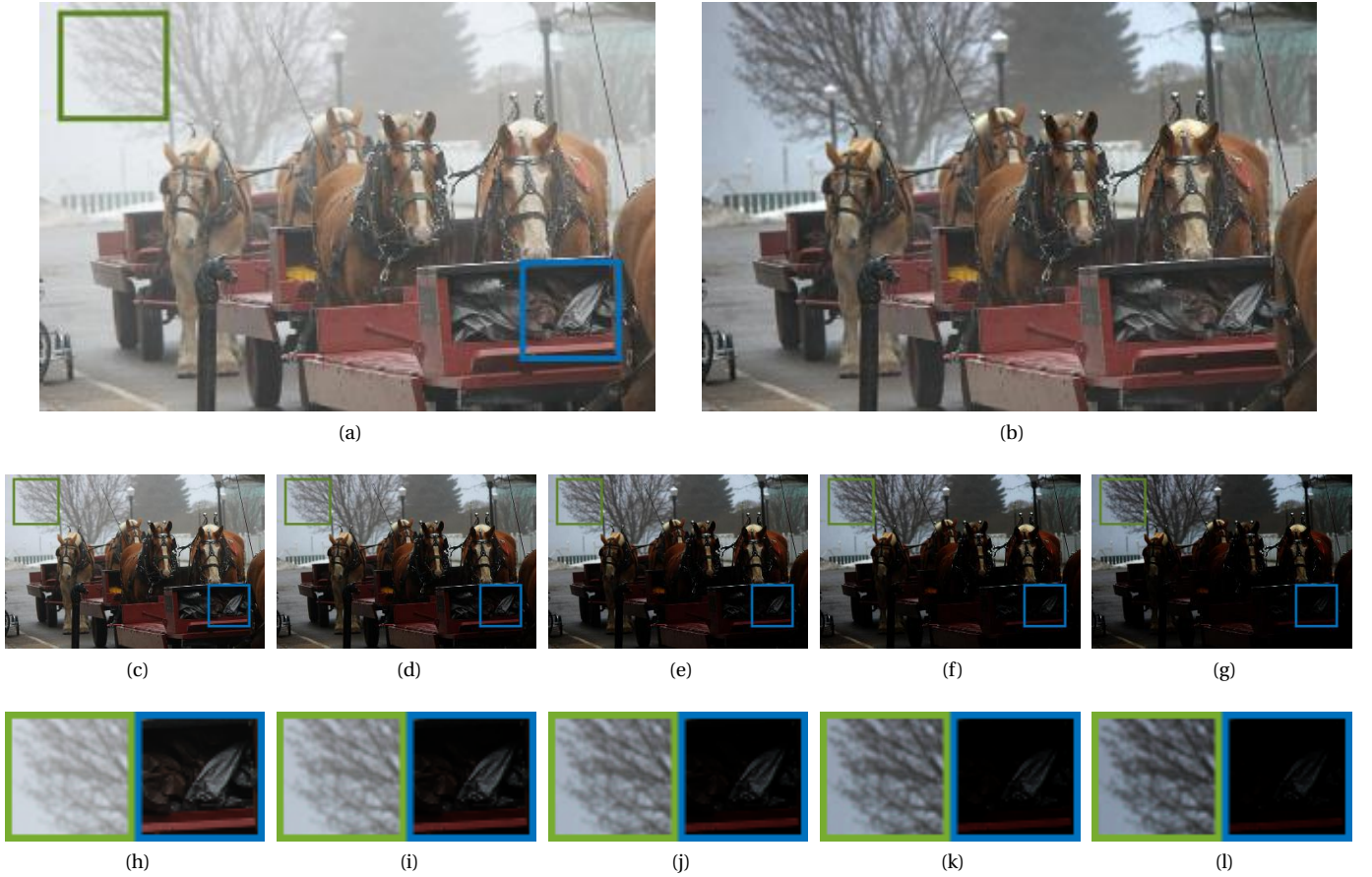
6

Figure 5: (a) Hazy image (b) Result of fusing multiple under-exposed versions of (a). (c)–(g) Progressively artificial under-exposing of the image in (a). (h)–(l) Zoomed-up details of: left) an initially hazy region that becomes better exposed right) an initially well-exposed region that becomes excessively under-exposed.

the amount of contrast the user allows to be increased in the adaptive histogram equalization image that complements the artificially under-exposed set of images, as explained above. A qualitative analysis of the influence of this parameter is provided below.

Concerning the remaining parameters, the selected set of artificial exposures was fixed as $\gamma \in \{1, 2, 3, 4, 5\}$ in the beginning of the experimental evaluation. Likewise, the smoothing kernel in eqs. (7) and (8) was set to a conventional separable filter given by $G = [1/16, 1/4, 3/8, 1/4, 1/16]$, and the number of levels N in the pyramid decomposition, which was automatically selected following the suggested method in [38] as $L = \dfrac{\log(\min(m, n))}{\log(2)}$, for an input image of size $m \times n$. Every result shown in this paper is obtained under this generic configuration.

Regarding the range of values that the adaptive histogram equalization is allowed to increase/decrease (*clip-range*, denoted c in the following), Fig. 7 shows a set of examples on which **AMEF** is computed with an increasing range of clip-range values, varying from $c = 0.03$ to $c = 0.2$. It can be observed how the contrast in the resulting dehazed image can be progressively increased by allowing a larger c value. Un-

fortunately, specifying a too high value of c may sometimes lead to a clear over-enhancing that, even if increasing visibility, may slightly distort the color distribution of the input hazy scene. It is worth noting, however, that even for small values of c **AMEF** already shows excellent fog removal capabilities. On the other hand, large values of c still share these capabilities but may modify regions that are close-by to the observer and need no enhancement. A safe choice of c balancing contrast enhancement with color preservation was experimentally found to be $c = 0.10$. This value provides good results and has been fixed in order to generate the dehazed images for the next section.

4.2. Subjective Evaluation

As a first example, in order to visually demonstrate that **AMEF** shares the same dehazing capabilities as the most well-performing fog removal techniques in the literature, an image of a hazy stadium is shown in Fig. 8. In this case, it can be seen that the methods with higher fog-removal ability are the DCP in Fig. (8g) and **AMEF** in Fig. (8i). Moreover, zoomed-up details of a far-away region within the stadium are provided in order for the reader to appreciate the effect of different dehazing techniques. From these cropped

Figure 6: Extraction of different regions from multiply-exposed areas of the input image and from its adaptively histogram-equalized version. (a) Input hazy image (b) Result of the proposed technique (c) Result of applying Contrast-Limited Adaptive Histogram Equalization to (a) (d)-(f) input image under-exposed with (d) $\gamma = 2$ (e) $\gamma = 3$ (f) $\gamma = 4$.

regions, it can observed in Fig. (8e) that the method proposed in [9], based on the Color Attenuation Prior, exhibits lower dehazing power than the DCP and **AMEF**. In addition, the technique from [44], which is an extension of the DCP, introduces in this case an unrealistic color shift, as can be seen in Fig. (8f). Lastly, the artifact-free dehazing technique proposed in [23] recovers a high saturation, but at the cost of losing some contrast and producing slightly blurred details, as observed in Fig. (8k).

A hazy scene depicting a street with fading visibility in the bottom is presented in Fig. (9). In this case the Bayesian defogging [45] and contrast maximization [12] methods seem to recover more contrast at the bottom of the scene. Unfortunately, this comes at the cost of a clear overenhacement and unnatural color distortions, as can be appreciated in the pavement color nearby the camera, which is substantially darkened. The machine-learning based technique from [46] manages to obtain a good detail visibility across the image, but the colors of closer objects are slightly distorted, whereas the artifact-free dehazing approach of [23] produces again slightly blurred results. On the other hand, the DCP [8] and the Color Attenuation Prior technique [9], together with **AMEF**,

are the techniques that better preserve the aspect of haze-free areas while retrieving more visibility.

In the next example, a hazy landscape is shown in Fig. (10). In this case, it can be appreciated that **AMEF** is capable of avoiding some of the color artifacts affecting other dehazing techniques, typically appearing when there is a varying illumination affecting the imaged scene. In this scene, the sun lies behind the clouds in the top rightmost area of the image in Fig. (10a). Its presence introduces a slowly-varying illumination that clearly affects the result in Fig. (10c), obtained by the technique proposed in [47], which estimates the transmission by means of a series of median filters. The same happens to the results shown in Figs. (10e) and (10f), produced respectively by the technique from [44] and the Optimized Contrast Enhancement approach of [48]. These two methods create artificial colors around the sun's position and across the rest of the image.

The landscape example of Fig. (10) is particularly relevant for the qualitative evaluation of different dehazing techniques, because the scene contains a large portion of sky, which is a well-known typical failure case for most fog removal methods. This is specially the case for those tech-
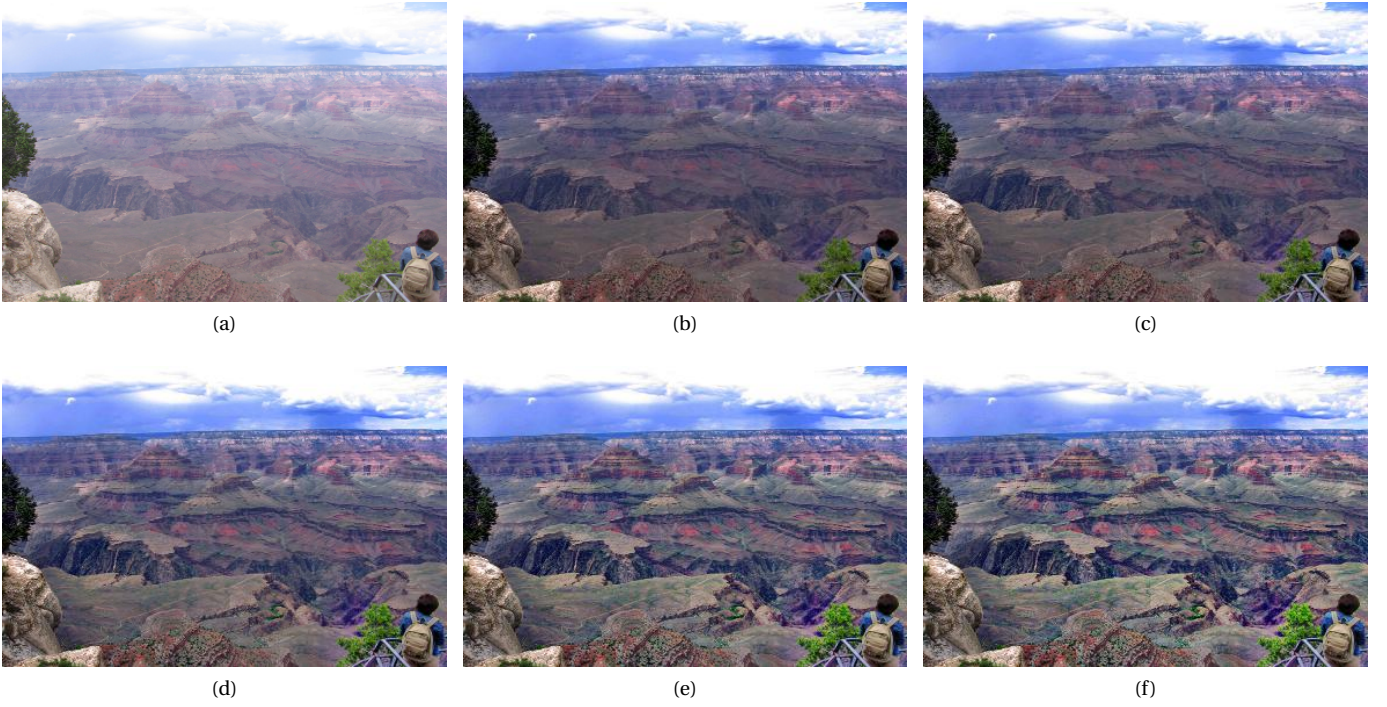
8

Figure 7: Influence of the clip-range parameter c on the behavior of the proposed technique. (a) Hazy landscape (b)–(f) Result of dehazing with (b) $c = 0.003$ (c) $c = 0.005$ (d) $c = 0.010$ (e) $c = 0.015$ (f) $c = 0.020$.
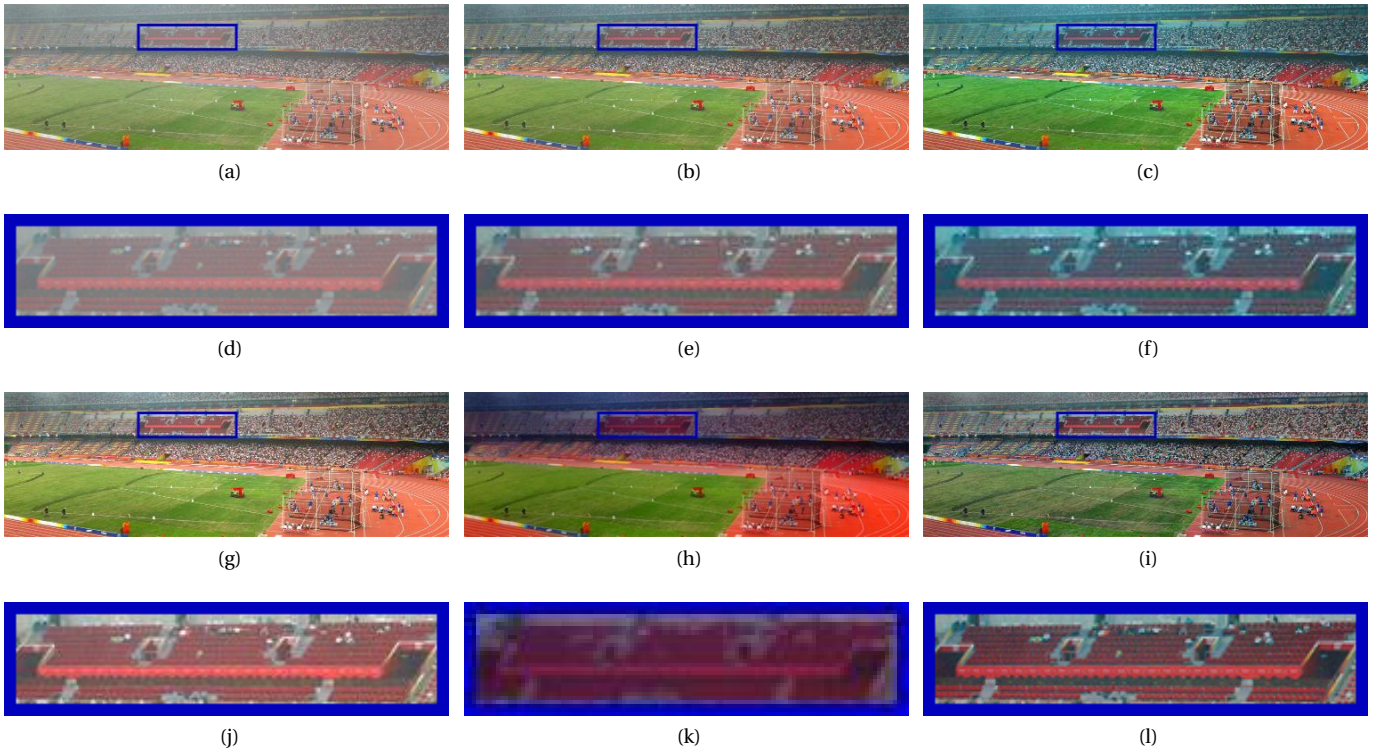

Figure 8: (a) A hazy stadium, and the results of processing it with the techniques introduced in: (b) Color Attenuation Prior [9] (c) Boundary-Constrained Contextual Regularization [44] (g) Dark Channel Prior [8] (h) Artifact-free dehazing [23] (i) **AMEF**. (d)–(f) and (j)–(l) contain zoomed-up details of the result produced by the respective techniques.

niques operating through patch-wise computations. For this   reason, even the DCP technique cannot succeed in augment-
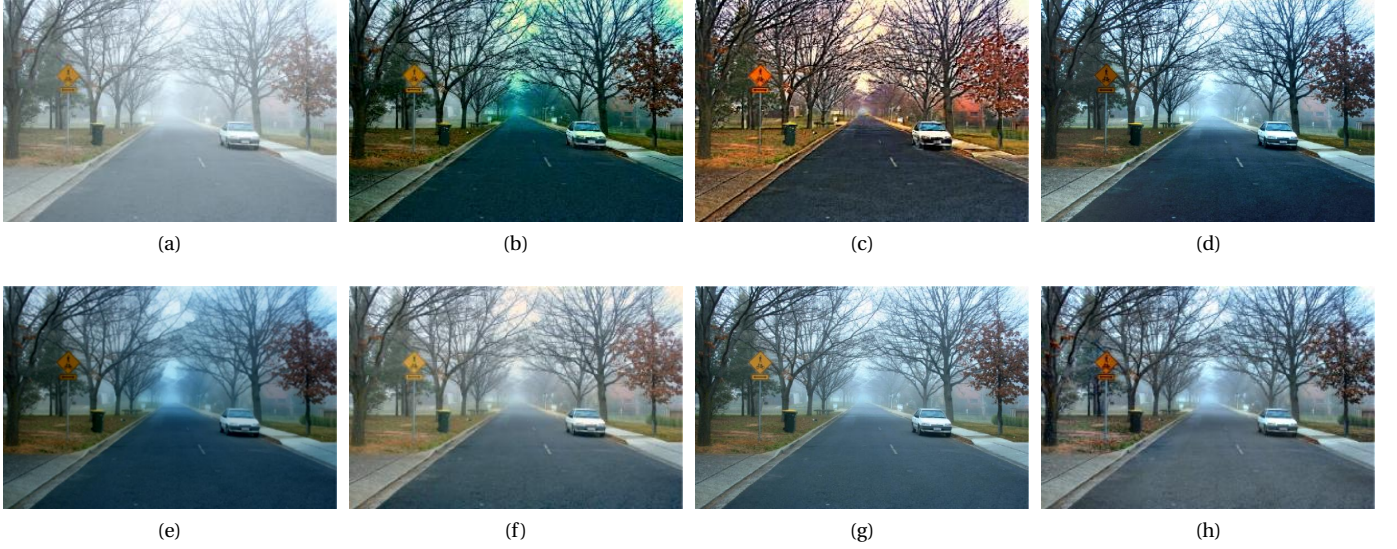
Figure 9: (a) Hazy street scene, and (b)–(h) the results of processing it with the techniques introduced in: (b) Bayesian Defogging [45] (c) Contrast Maximization [12] (d) FADE [46] (e) Artifact-free dehazing [23] (f) DCP [8] (g) Color Attenuation Prior [9] (h) **AMEF**.

ing the visibility of the mountains that appear in the horizon, producing a yellowish unnatural chromatic artifact, as illustrated in Fig. (10g). It is worth noting that the Guided Filter-based technique from [49] and **AMEF** can both handle better the sky region without creating that kind of artifact. At the same time, both methods considerably increase the visibility of far away areas. However, the former achieves this at the cost of losing brightness in the closer areas of the scene, which become too dark and unnaturally saturated, as seen Fig. (10b). On the contrary, **AMEF** behaves satisfactorily, handling correctly both far-away and close-by regions, as shown in (10h). In this example it can also be observed that, thanks to the contribution of the Contrast-Limited Adaptive Histogram Equalization, even areas of the input that were initially under-exposed – see bottom part of Fig. (10a) – can also be enhanced by **AMEF**.

4.3. Quantitative Evaluation

There exist two main ways to provide an objective evaluation of a dehazing technique. First, a full-reference score can be employed to compare a foggy image with a corresponding haze-free image acting as ground-truth. Second, a no-reference image quality metric can be applied to quantify the level of enhancement that a given method achieves. In the next sections we follow these two types of performance analysis, providing comparisons of the proposed **AMEF** technique with a wide range of other image dehazing approaches.

4.3.1. Full-Reference Image Quality Assessment

For the computation of a full-reference quality score, it is assumed that hazy images with corresponding haze-free versions are available. After the hazy image has been processed, it can be compared with the undegraded image in

order to understand if contrast at foggy areas has been properly increased. Unfortunately, it is extremely difficult to obtain clean and corresponding weather-degraded images of the same scene. Even if a camera acquires pictures of a scene under varying weather conditions, external factors, such as the illumination or moving objects, may render a full-reference comparison in this scenario useless.

In order to enable a full-reference performance comparison of **AMEF** with different dehazing techniques in terms of the degree of retrieved contrast and saturation, we follow the same approach as in [51, 52, 53], *i.e.* we build a dataset of images in which synthetically generated fog is added. To achieve this, the LIVE Color+3D Database is used [54], since it contains ground-truth depth information. This data was obtained with a range scanner and a digital camera mounted on top of it. The database includes twelve different scenes together with corresponding real depth data for each of them.

For the injection of realistic fog layers on top of the LIVE Color+3D images, we employed the software provided in [51] to synthesize haze in four different variants. This is accomplished by a modification of eq. (1) to introduce variability on its different terms. In this way, random Perlin noise is added to the transmission $t(x)$ and the airlight **A**. The resulting dataset, referred to as LIVE-hazy in the following, contains a foggy version for each image in LIVE Color+3D, namely: 1) homogeneous airlight and transmission fog, heterogeneous airlight and homogeneous transmission fog, homogeneous airlight and heterogeneous transmission fog, and heterogeneous airlight and transmission fog. A sample of an image in LIVE Color+3D and the corresponding foggy images generated with these four different haze types is provided in Fig. 11.

Next, **AMEF** is compared versus several current state-of-the-art dehazing techniques. In this analysis, the following
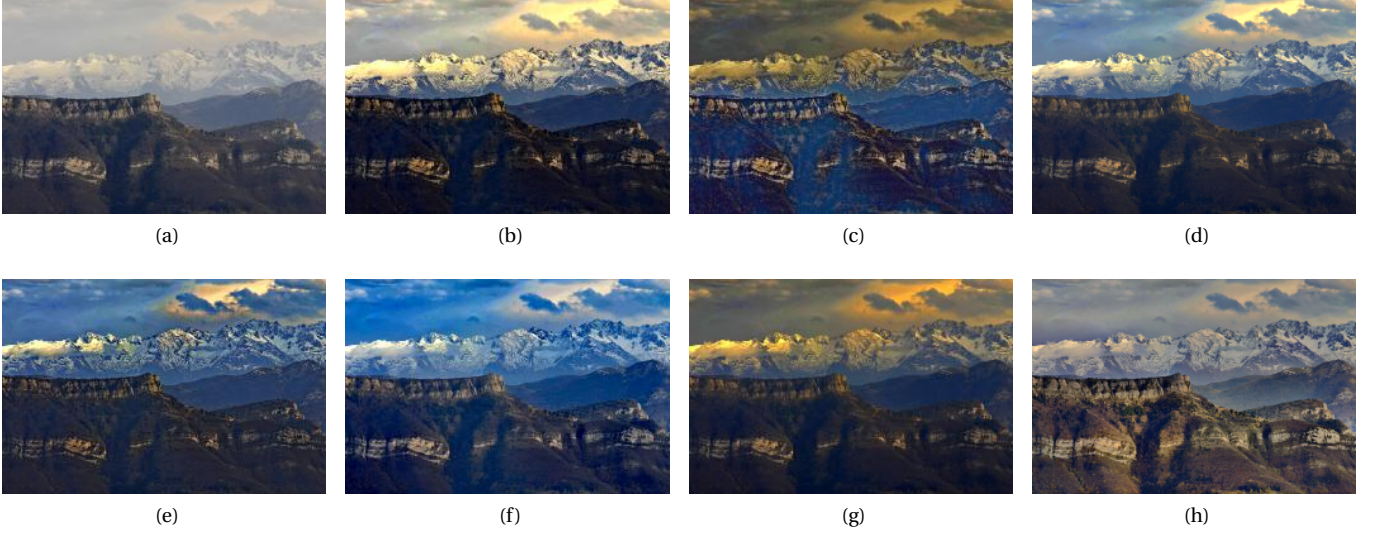
Figure 10: (a) Hazy mountains image (b)-(h) Processed by the techniques introduced in (b) Guided Joint Bilateral Filter [49] (c) Fast median filter for transmission estimation [47] (d) Haze-relevant Features [16] (e) Boundary-Constrained Contextual Regularization [44] (f) [48] Optimized Contrast Enhancement (g) DCP [8] (h) **AMEF**. Original hazy scene and all processed images were extracted from [50].
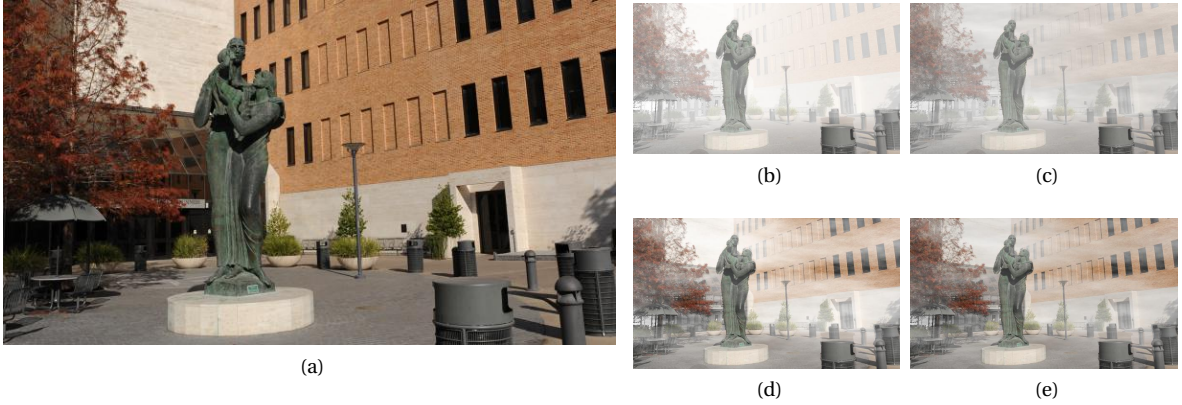

Figure 11: (a) Original Image (b) Homogeneous Fog added (c) Fog of heterogeneous airlight added (d) Fog of heterogeneous attenuation added (e) Fog of both heterogeneous airlight and attenuation added.

methods are included: 1. Dark Channel Prior (**DCP**) [8], 2. Enhanced Variational Image Dehazing (**EVID**) [52], 3. Fusion-Based Variation Image Dehazing (**FVID**) [22], 4. Fast Visibility Restoration (**FVR**) [47], 5. Boundary-Constrained and Contextual Regularization (**BCCR**) [44], 6. Density of Fog Assessment-based Defogger (**DEFADE**) [46], 7. Color Attenuation Prior (**CAP**) [9], 8. Robust Artifact Suppression Dehazing (**RAS**) [23]. A comparison with Contrast Limited Adaptive Histogram Equalization (**CLAHE**) [43] is also performed, since it is of interest to observe if **AMEF** can obtain better performance than a technique that is included into the set of images that it combines. For CLAHE, Matlab® implementation with default values (clip range $c = 0.01$) was applied.

After dehazing all the 48 synthetic foggy images with **AMEF** and the aforementioned image dehazing techniques, the well-known Structual Similarity error [55] between the reference image and the dehazed one is computed. In this case, we found that a well-performing clip-range parameter for **AMEF** was $c = 0.03$. The mean SSIM error for all images is reported in Table 1. It can be appreciated that **AMEF** is capable of removing fog of different types to the same extent as other popular image dehazing techniques, obtaining the second best average SSIM error, only behind the DCP technique. It is also worth noting the large difference in performance, between CLAHE and **AMEF**, which verifies that the combination of a contrast-enhanced image and the set of multi-exposed images performs much better than simple local contrast enhancement.

4.3.2. No-Reference Image Quality Assessment

A wide range of no-reference image quality assessment scores is available in the image processing literature, either generic or designed to measure different image degradations. However, it has been recently shown in [50] that most of these

Table 1: SSIM performance comparison of **AMEF** and other image dehazing techniques on the LIVE-hazy dataset. Results sorted in ascending performance. Best method is marked **green**, second best is marked **orange**, and third best is marked **red**.

Method	Mean SSIM Error	Short Explanation
RASD [23]	0.507	Robust Artifact-Supression Dehazing
CLAHE [43]	0.671	Contrast-Limited Adaptive Histogram Equalization
CAP [9]	0.708	Imposes Color Attenuation Prior
DEFADE [46]	0.716	Learned Model of Fog presence + Fusion Scheme
FVID [22]	0.762	Fusion of the Iterates from EVID
FVR [47]	0.774	Fast Median Filter for Transmission Estimate
EVID [52]	0.780	Iterative Variational Image Dehazing
BCCR [44]	**0.792**	Contextual Transmission Regularization
DCP [8]	**0.807**	Imposes Dark Channel Prior
AMEF	**0.795**	**Artificial Multiple Exposure Fusion.**

quality metrics fail to capture the subjective opinion of human observers regarding image appearance when evaluating image dehazing techniques. Accordingly, to evaluate the dehazing capability of different techniques when compared to **AMEF**, we apply the Fog Aware Density Evaluator (FADE) metric, introduced in [46], which is specifically designed for assessing image dehazing techniques. FADE is a learned quality metric, supported by the computation of a set of fog-aware features across two sets of images, foggy and fog-free, each of them containing 500 images. We selected the first set of hazy images on which FADE was trained to compare the performance of the different techniques. This dataset is publicly available [1]. Results of the mean FADE values scored across the considered 500 images, after processing them with the same set of dehazing techniques as in previous section, are shown in Table 2.

First, it is important to remark that the best-performing clip-range value for **AMEF** in this case was found to be $c = 0.20$. However, it must be noted that the FADE metric tends to slightly reward an increased saturation, which agrees with the better-performing greater clip-range value. Second, an analysis of the performances reported in Table 2 reveals that CLAHE performs substantially worse than **AMEF** also by this metric, obtaining even a lower score than the original hazy images, which confirms that simple local contrast enhancement is not enough to remove fog effects. Also, it is important to emphasize that the best performing technique under the FADE metric is the DEFADE method [46]. This is a machine learning technique that was trained employing the same dataset on which these scores are computed. As a consequence, it is natural to expect a particularly good performance of DEFADE regarding this quality score. In this case, **AMEF** scores again the second best position, verifying its good dehazing capability also when measured by a specialized no-reference quality metric.

For reference, we also include in Table 2 the result of computing a no-reference quality metric designed for generic natural images, CORNIA (Codebook Representation for No-Reference Image Assessment) [56]. In this case, we did not modify the default value of the clip-range parameter, which was kept as $c = 0.10$. We can see that **AMEF** still performs among the best top image dehazing algorithms, ranking in the third position.

4.4. Computational Performance Analysis

One critical aspect of image dehazing techniques is the execution time the algorithm needs in order to process an image. In this section we provide a computational performance study to demonstrate the ability of **AMEF** to remove haze efficiently. In this analysis we consider some of the dehazing techniques mentioned in Section 4.3.1. In addition, we incorporate to the analysis the Image Dehazing by Multi-Scale Fusion (**MSF**) technique from [21], the Visibility in Bad Weather (**VBW**) method from [12], the Single Image Dehazing (**SID**) technique introduced in [57], the Color-Lines (**C-Lines**) approach from [13], the Non-Local Image Dehazing (**NLID**) technique proposed in [14], the Haze-Relevant Feature analysis (**HRF**) method from [16], and the Dehazenet Convolutional Neural Network (**DHZNet**) introduced in [18]. The resulting execution times for all these different techniques, extracted from [15][2], are reported in Table 3.

4.5. Robustness to JPEG compression artifacts

Another key aspect of image dehazing techniques is their ability to deal with compression artifacts that typically appear on large bright areas with few contrast, *e.g.* white buildings, portions of sky, etc. This is a typical failure scenario for image dehazing techniques that carry out a per-patch

---

[1]Accessible at http://live.ece.utexas.edu/research/fog/fade_defade.html

[2]Experiments in this reference were run using a desktop with a Xeon E5 3.5GHz CPU and 16GB of RAM. Runtimes for **FVID** and **AMEF** were obtained by running the methods locally, in a desktop computer of the same specifications.

Table 2: Quantitative results of the FADE score on a dataset of 500 hazy images. A lower FADE score implies less quantity of fog. Best method is marked **green**, second best is marked **orange**, and third best is marked **red**.

Method	None	CLAHE [43]	CAP [9]	FVID [22]	DCP [8]	
FADE	1.6335	1.850	1.048	0.930	0.870	
CORNIA	22.002	23.329	28.538	29.486	23.592	
Method	**FVR** [47]	**EVID** [52]	**RASD** [23]	**BCCR** [44]	**DEFADE** [46]	**AMEF**
FADE	0.748	0.691	0.625	**0.564**	**0.517**	**0.5597**
CORNIA	24.002	23.707	**32.069**	**35.264**	24.057	**30.156**

processing, like the Dark Channel method [8], and several fog removal methods specifically dealing with this issue have been proposed before. In [58], the authors applied an initial texture-structure decomposition of the hazy image and dehazing was only performed in the structure layer. In [23], the authors noticed that the technique proposed in [58] could remove compression artifacts but it was unable to handle other kinds of degradation typical of image dehazing processes, like color shifting or color aliasing. A new technique was proposed to deal with these artifacts, consisting of imposing a Generalized Total Variation regularization on the depth map of the scene in order to obtain transmission maps on which object surfaces were smooth whereas depth jumps corresponded to strong edge discontinuities. The method could this way remove typical JPEG artifacts that arise as a consequence of trying to unnecessarily boost contrast on large texture-less areas.

In Fig. 12, we show an example of a challenging image, in which there is a large region of sky and also white buildings. The result of the Dark Channel method and of the techniques from [58, 23] is compared with the output of **AMEF**. We can clearly see in Figs. 12b and the zoomed-up detail on Fig. 12g that the Dark Channel Prior, when imposed on such areas, makes JPEG artifacts much more visible and also introduces a color shift in the sky area, while at the same time being slightly unable to recover the contrast of the white facade, where some windows disappear. On the contrary, the technique from [58] is capable of reducing the compression artifacts, although the color shift persists, as observed in Fig. 12h. This inability of the method from [58] to remove color shift degradation was already noticed and dealt with in [23]. The image dehazing from this work obtains a better result in terms of color and compression artifacts in this case, see Figs. 12d and 12i. Unfortunately, due to the Total Variation

Prior imposed in the result, much of the detail in the building facade is removed, and only prominent edges are preserved. When compared with these, the result produced by **AMEF** is more satisfactory: higher visibility is retrieved in the buildings' region, whereas no color shift is introduced, and the compression artifacts produced by the Dark Channel Prior are removed in this case, as can be seen in Figs. 12e and 12j.

5. Conclusions and Future Work

A new image dehazing technique, termed **AMEF**, has been developed. **AMEF** is based on the multi-scale fusion of a set of progressively over-exposed versions of the initial hazy image. It is important to notice that other fusion-based approaches to image dehazing have been proposed in the past, namely [21] or [22]. In comparison to these techniques, **AMEF** can perform fog removal by considering simpler visual features from the input image: **AMEF** considers only contrast and saturation as quantities of interest, while [22] combines partial images coming from a computationally expensive external iterative process that minimizes a separate image energy, and [21] is supported by the estimation of luminance, chromaticity, and visual saliency maps from a hazy image. In addition, **AMEF** is partially inspired on a haze image formation model to select the images that are fed to the a multi-scale fusion process, while avoiding to invert said model. Since a hazy image contains brighter intensities with loss of contrast and saturation, **AMEF** is designed to find better contrasted/saturated regions from artificially under-exposed versions of the input image. As a consequence of these characteristics of the proposed algorithm, we obtain an image dehazing technique that can produce images of improved quality, and in a more efficient way: **AMEF** is the fastest among all the techniques considered in this paper, including fusion-based approaches. **AMEF** has been validated extensively through

Table 3: Average runtime tested on images of 720×480 resolution. Fastest method is marked **green**, second fastest is marked **orange**, and third fastest is marked **red**.

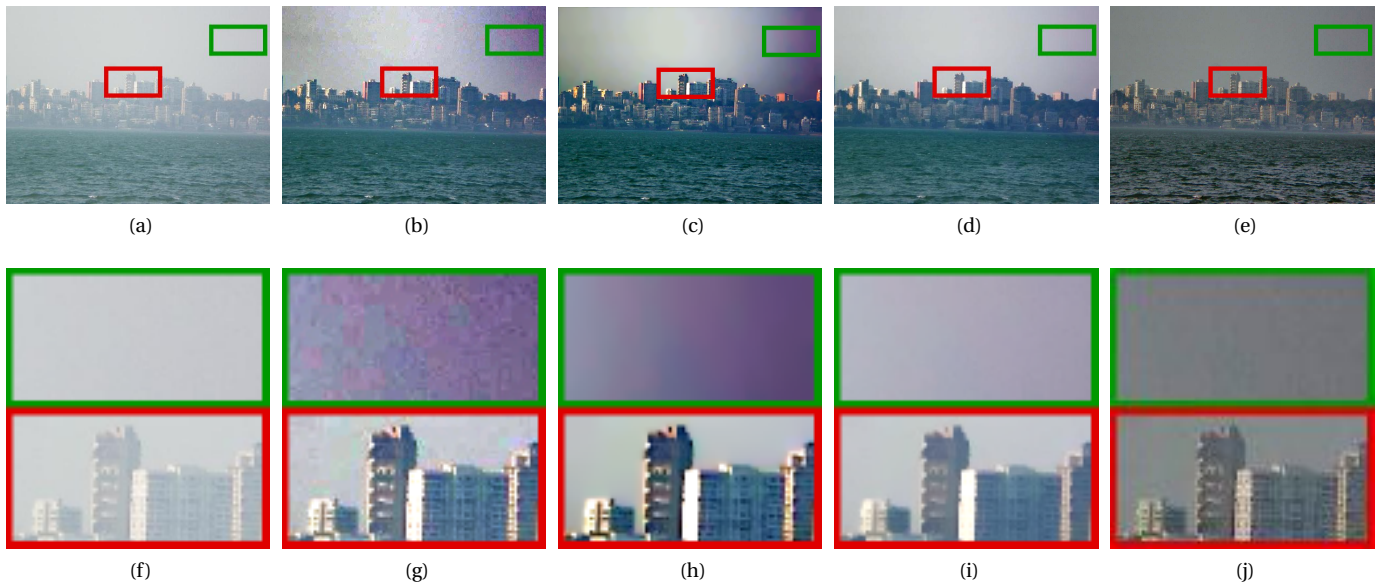| Method	MSF [21]	VBW [12]	SID [57]	DCP [8]	FVR [47]	FVID	
Runtime	3.0	3.3	141.1	20	12.8	30.0	
Method	**BYD** [45]	**BCCR** [44]	**C-Lines** [13]	**NLID** [14]	**HRF** [16]	**DHZNet** [18]	**AMEF**
Runtime	124.2	**1.0**	1.9	**1.8**	10.4	1.7	**0.7**

Figure 12: (a)Input hazy image containing a large piece of sky and several white buildings. (b)–(e) Processed by the techniques introduced in (b) [8] (c) [58] (d) [23] (e) **AMEF** (f)–(j) Zoomed-up details where the reader can appreciate the ability of each method to handle compression artifacts while still producing an appropriate amount of contrast on hazy areas.

a series of qualitative and quantitative experiments, revealing that it competes well and can outperform most current state-of-the-art techniques. The method has been shown to be robust, efficient, and capable of correctly removing the visual effect of haze on images acquired under a variety of bad-weather conditions, correctly handling compression artifacts.

AMEF exhibits a good performance for the task of image dehazing. However, the idea of generating artificially exposed versions of a poor-quality image and merge them into an output of better visual quality is not limited to the task of fog removal. Other image processing problems, such as uneven illumination compensation, may benefit from a similar approach. Moreover, the applied multi-scale Laplacian image fusion scheme is a basic technique within the field of multiple-exposure image fusion, and more advanced methods could be explored to further improve performance or investigate other applications.

Acknowledgment

References

[1] Y. Cheng, W. Niu, Z. Zhai, Video dehazing for surveillance unmanned aerial vehicle, in: 2016 IEEE/AIAA 35th Digital Avionics Systems Conference (DASC), 2016, pp. 1–5. doi:10.1109/DASC.2016.7777960.

[2] M. S. Al-Rawi, A. Galdran, X. Yuan, M. Eckert, J. F. Martinez, F. Elmgren, B. Cürüklü, J. Rodriguez, J. Bastos, M. Pinto, Intensity normalization of sidescan sonar imagery, in: 2016 Sixth International Conference on Image Processing Theory, Tools and Applications (IPTA), 2016, pp. 1–6. doi:10.1109/IPTA.2016.7820967.

[3] Q. Liu, X. Gao, L. He, W. Lu, Haze removal for a single visible remote sensing image, Signal Processing 137 (2017) 33–43. doi:10.1016/j.sigpro.2017.01.036.

[4] N. Hautiere, J. P. Tarel, D. Aubert, Towards Fog-Free In-Vehicle Vision Systems through Contrast Restoration, in: 2007 IEEE Conference on Computer Vision and Pattern Recognition, 2007, pp. 1–8. doi:10.1109/CVPR.2007.383259.

[5] S. G. Narasimhan, S. K. Nayar, Contrast restoration of weather degraded images, IEEE Transactions on Pattern Analysis and Machine Intelligence 25 (6) (2003) 713–724. doi:10.1109/TPAMI.2003.1201821.

[6] Y. Y. Schechner, S. G. Narasimhan, S. K. Nayar, Polarization-based vision through haze, Applied Optics 42 (3) (2003) 511–525. doi:10.1364/AO.42.000511.

[7] J. Kopf, B. Neubert, B. Chen, M. Cohen, D. Cohen-Or, O. Deussen, M. Uyttendaele, D. Lischinski, Deep Photo: Model-based Photograph Enhancement and Viewing, in: ACM SIGGRAPH Asia 2008 Papers, SIGGRAPH Asia '08, ACM, New York, NY, USA, 2008, pp. 116:1–116:10. doi:10.1145/1457515.1409069.

[8] K. He, J. Sun, X. Tang, Single Image Haze Removal Using Dark Channel Prior, IEEE Transactions on Pattern Analysis and Machine Intelligence 33 (12) (2011) 2341–2353. doi:10.1109/TPAMI.2010.168.

[9] Q. Zhu, J. Mai, L. Shao, A Fast Single Image Haze Removal Algorithm Using Color Attenuation Prior, IEEE Transactions on Image Processing 24 (11) (2015) 3522–3533. doi:10.1109/TIP.2015.2446191.

[10] H. Koschmieder, Theorie der horizontalen sichtweite: kontrast und sichtweite, Keim & Nemnich, 1925.

[11] S. Lee, S. Yun, J.-H. Nam, C. S. Won, S.-W. Jung, A review on dark channel prior based image dehazing algorithms, EURASIP Journal on Image and Video Processing 2016 (1) (2016) 4. doi:10.1186/s13640-016-0104-y.

[12] R. T. Tan, Visibility in bad weather from a single image, in: 2008 IEEE Conference on Computer Vision and Pattern Recognition, 2008, pp. 1–8. doi:10.1109/CVPR.2008.4587643.

[13] R. Fattal, Dehazing Using Color-Lines, ACM Trans. Graph. 34 (1) (2014) 13:1–13:14. `doi:10.1145/2651362`.

[14] D. Berman, T. Treibitz, S. Avidan, Non-local Image Dehazing, in: 2016 IEEE Conference on Computer Vision and Pattern Recognition (CVPR), 2016, pp. 1674–1682. `doi:10.1109/CVPR.2016.185`.

[15] Y. Li, S. You, M. S. Brown, R. T. Tan, Haze visibility enhancement: A Survey and quantitative benchmarking, Computer Vision and Image Understanding`doi:10.1016/j.cviu.2017.09.003`.
URL `http://www.sciencedirect.com/science/article/pii/S1077314217301595`

[16] K. Tang, J. Yang, J. Wang, Investigating Haze-Relevant Features in a Learning Framework for Image Dehazing, in: 2014 IEEE Conference on Computer Vision and Pattern Recognition, 2014, pp. 2995–3002. `doi:10.1109/CVPR.2014.383`.

[17] W. Ren, S. Liu, H. Zhang, J. Pan, X. Cao, M.-H. Yang, Single Image Dehazing via Multi-scale Convolutional Neural Networks, in: Computer Vision – ECCV 2016, Lecture Notes in Computer Science, Springer, Cham, 2016, pp. 154–169. `doi:10.1007/978-3-319-46475-6_10`.

[18] B. Cai, X. Xu, K. Jia, C. Qing, D. Tao, DehazeNet: An End-to-End System for Single Image Haze Removal, IEEE Transactions on Image Processing 25 (11) (2016) 5187–5198. `doi:10.1109/TIP.2016.2598681`.

[19] A. Galdran, A. Alvarez-Gila, A. Bria, J. Vazquez-Corral, M. Bertalmío, On the Duality Between Retinex and Image Dehazing, accepted, in: 2018 IEEE Conference on Computer Vision and Pattern Recognition, Salt Lake City (USA), 2018.

[20] V. W. D. Dravo, J. Y. Hardeberg, Stress for dehazing, in: 2015 Colour and Visual Computing Symposium (CVCS), 2015, pp. 1–6. `doi:10.1109/CVCS.2015.7274895`.

[21] C. Ancuti, C. Ancuti, Single Image Dehazing by Multi-Scale Fusion, IEEE Transactions on Image Processing 22 (8) (2013) 3271–3282.

[22] A. Galdran, J. Vazquez-Corral, D. Pardo, M. Bertalmío, Fusion-Based Variational Image Dehazing, IEEE Signal Processing Letters 24 (2) (2017) 151–155. `doi:10.1109/LSP.2016.2643168`.

[23] C. Chen, M. N. Do, J. Wang, Robust Image and Video Dehazing with Visual Artifact Suppression via Gradient Residual Minimization, in: Computer Vision – ECCV 2016, Lecture Notes in Computer Science, Springer, Cham, 2016, pp. 576–591. `doi:10.1007/978-3-319-46475-6_36`.

[24] S. C. Huang, F. C. Cheng, Y. S. Chiu, Efficient Contrast Enhancement Using Adaptive Gamma Correction With Weighting Distribution, IEEE Transactions on Image Processing 22 (3) (2013) 1032–1041. `doi:10.1109/TIP.2012.2226047`.

[25] S. Rahman, M. M. Rahman, M. Abdullah-Al-Wadud, G. D. Al-Quaderi, M. Shoyaib, An adaptive gamma correction for image enhancement, EURASIP Journal on Image and Video Processing 2016 (1) (2016) 35. `doi:10.1186/s13640-016-0138-1`.

[26] Z. Huang, T. Zhang, Q. Li, H. Fang, Adaptive gamma correction based on cumulative histogram for enhancing near-infrared images, Infrared Physics & Technology 79 (2016) 205–215. `doi:10.1016/j.infrared.2016.11.001`.

[27] Y. Xiong, K. Pulli, Color matching of image sequences with combined gamma and linear corrections, in: International Conference on ACM Multimedia, 2010.

[28] S. C. Huang, B. H. Chen, W. J. Wang, Visibility Restoration of Single Hazy Images Captured in Real-World Weather Conditions, IEEE Transactions on Circuits and Systems for Video Technology 24 (10) (2014) 1814–1824. `doi:10.1109/TCSVT.2014.2317854`.

[29] S. C. Huang, J. H. Ye, B. H. Chen, An Advanced Single-Image Visibility Restoration Algorithm for Real-World Hazy Scenes, IEEE Transactions on Industrial Electronics 62 (5) (2015) 2962–2972. `doi:10.1109/TIE.2014.2364798`.

[30] Y. Gao, H.-M. Hu, S. Wang, B. Li, A fast image dehazing algorithm based on negative correction, Signal Processing 103 (2014) 380–398. `doi:10.1016/j.sigpro.2014.02.016`.

[31] M. Bertalmío, Image Processing for Cinema, 1st Edition, Chapman and Hall/CRC, Boca Raton, 2014.

[32] H. Farid, Blind inverse gamma correction, IEEE Transactions on Image Processing 10 (10) (2001) 1428–1433. `doi:10.1109/83.951529`.

[33] J. Vazquez-Corral, M. Bertalmío, Simultaneous Blind Gamma Estimation, IEEE Signal Processing Letters 22 (9) (2015) 1316–1320. `doi:10.1109/LSP.2015.2396299`.

[34] P. J. Burt, The Pyramid as a Structure for Efficient Computation, in: Multiresolution Image Processing and Analysis, Springer Series in Information Sciences, Springer, Berlin, Heidelberg, 1984, pp. 6–35, dOI: 10.1007/978-3-642-51590-3_2.
URL `https://link.springer.com/chapter/10.1007/978-3-642-51590-3_2`

[35] A. A. Goshtasby, Fusion of Multi-exposure Images, Image Vision Comput. 23 (6) (2005) 611–618. `doi:10.1016/j.imavis.2005.02.004`.

[36] K. Ma, H. Li, H. Yong, Z. Wang, D. Meng, L. Zhang, Robust Multi-Exposure Image Fusion: A Structural Patch Decomposition Approach, IEEE Transactions on Image Processing 26 (5) (2017) 2519–2532. `doi:10.1109/TIP.2017.2671921`.

[37] P. J. Burt, R. J. Kolczynski, Enhanced image capture through fusion, in: 1993 (4th) International Conference on Computer Vision, 1993, pp. 173–182. `doi:10.1109/ICCV.1993.378222`.

[38] T. Mertens, J. Kautz, F. V. Reeth, Exposure Fusion, in: 15th Pacific Conference on Computer Graphics and Applications, 2007. PG '07, 2007, pp. 382–390. `doi:10.1109/PG.2007.17`.

[39] B. Gu, W. Li, J. Wong, M. Zhu, M. Wang, Gradient field multi-exposure images fusion for high dynamic range image visualization, Journal of Visual Communication and Image Representation 23 (4) (2012) 604–610. `doi:10.1016/j.jvcir.2012.02.009`.

[40] S. Raman, S. Chaudhuri, Bilateral filter based compositing for variable exposure photography, in: Short Papers, Eurographics, 2009, pp. 1–4.

[41] S. Li, X. Kang, J. Hu, Image Fusion With Guided Filtering, IEEE Transactions on Image Processing 22 (7) (2013) 2864–2875. `doi:10.1109/TIP.2013.2244222`.

[42] P. Burt, E. Adelson, The Laplacian Pyramid as a Compact Image Code, IEEE Transactions on Communications 31 (4) (1983) 532–540. `doi:10.1109/TCOM.1983.1095851`.

[43] K. Zuiderveld, Graphics Gems IV, Academic Press Professional, Inc., San Diego, CA, USA, 1994, pp. 474–485.

[44] G. Meng, Y. Wang, J. Duan, S. Xiang, C. Pan, Efficient Image Dehazing with Boundary Constraint and Contextual Regularization, in: Proceedings of the 2013 IEEE International Conference on Computer Vision, ICCV '13, IEEE Computer Society, Washington, DC, USA, 2013, pp. 617–624. `doi:10.1109/ICCV.2013.82`.

[45] K. Nishino, L. Kratz, S. Lombardi, Bayesian Defogging, International Journal of Computer Vision 98 (3) (2012) 263–278. `doi:10.1007/s11263-011-0508-1`.

[46] L. K. Choi, J. You, A. C. Bovik, Referenceless Prediction of Perceptual Fog Density and Perceptual Image Defogging, IEEE Transactions on Image Processing 24 (11) (2015) 3888–3901. `doi:10.1109/TIP.2015.2456502`.

[47] J. P. Tarel, N. Hautière, Fast visibility restoration from a single color or gray level image, in: 2009 IEEE 12th International Conference on Computer Vision, 2009, pp. 2201–2208. `doi:10.1109/ICCV.2009.5459251`.

[48] J.-H. Kim, W.-D. Jang, J.-Y. Sim, C.-S. Kim, Optimized contrast enhancement for real-time image and video dehazing, Journal of Visual Communication and Image Representation 24 (3) (2013) 410–425. `doi:10.1016/j.jvcir.2013.02.004`.

[49] C. Xiao, J. Gan, Fast image dehazing using guided joint bilateral filter, The Visual Computer 28 (6-8) (2012) 713–721. `doi:10.1007/s00371-012-0679-y`.

[50] K. Ma, W. Liu, Z. Wang, Perceptual evaluation of single image dehazing algorithms, in: 2015 IEEE International Conference on Image Processing (ICIP), 2015, pp. 3600–3604. `doi:10.1109/ICIP.2015.7351475`.

[51] J. P. Tarel, N. Hautiere, L. Caraffa, A. Cord, H. Halmaoui, D. Gruyer, Vision Enhancement in Homogeneous and Heterogeneous Fog, IEEE Intelligent Transportation Systems Magazine 4 (2) (2012) 6–20. `doi:10.1109/MITS.2012.2189969`.

[52] A. Galdran, J. Vazquez-Corral, D. Pardo, M. Bertalmío, Enhanced Variational Image Dehazing, SIAM Journal on Imaging Sciences 8 (3) (2015) 1519–1546. `doi:10.1137/15M1008889`.

[53] C. Ancuti, C. O. Ancuti, C. D. Vleeschouwer, D-HAZY: A dataset to evaluate quantitatively dehazing algorithms, in: 2016 IEEE International Conference on Image Processing (ICIP), 2016, pp. 2226–2230.

15

`doi:10.1109/ICIP.2016.7532754`.

[54] C. C. Su, L. K. Cormack, A. C. Bovik, Color and Depth Priors in Natural Images, IEEE Transactions on Image Processing 22 (6) (2013) 2259–2274. `doi:10.1109/TIP.2013.2249075`.

[55] Z. Wang, A. C. Bovik, H. R. Sheikh, E. P. Simoncelli, Image quality assessment: from error visibility to structural similarity, IEEE Transactions on Image Processing 13 (4) (2004) 600–612. `doi:10.1109/TIP.2003.819861`.

[56] P. Ye, J. Kumar, L. Kang, D. Doermann, Unsupervised feature learning framework for no-reference image quality assessment, in: 2012 IEEE Conference on Computer Vision and Pattern Recognition, 2012, pp. 1098–1105. `doi:10.1109/CVPR.2012.6247789`.

[57] R. Fattal, Single Image Dehazing, in: ACM SIGGRAPH 2008 Papers, SIGGRAPH '08, ACM, New York, NY, USA, 2008, pp. 72:1–72:9. `doi:10.1145/1399504.1360671`.
URL `http://doi.acm.org/10.1145/1399504.1360671`

[58] Y. Li, F. Guo, R. T. Tan, M. S. Brown, A Contrast Enhancement Framework with JPEG Artifacts Suppression, in: Computer Vision – ECCV 2014, Lecture Notes in Computer Science, Springer, Cham, 2014, pp. 174–188. `doi:10.1007/978-3-319-10605-2_12`.